

Article

Pentacoordinate and Hexacoordinate Mn(III) Complexes of Tetradentate Schiff-Base Ligands Containing Tetracyanidoplatinate(II) Bridges and Revealing Uniaxial Magnetic Anisotropy

Ivan Nemeč, Radovan Herchel and Zdeněk Trávníček *

Department of Inorganic Chemistry, Faculty of Science, Palacký University, 17. listopadu 12, CZ-771 46 Olomouc, Czech Republic; ivan.nemec@upol.cz (I.N.); radovan.herchel@upol.cz (R.H.)

* Correspondence: zdenek.travnicsek@upol.cz; Tel.: +420-585-634-352

Academic Editor: Derek J. McPhee

Received: 25 October 2016; Accepted: 2 December 2016; Published: 8 December 2016

Abstract: Crystal structures and magnetic properties of polymeric and trinuclear heterobimetallic $\text{Mn}^{\text{III}} \dots \text{Pt}^{\text{II}} \dots \text{Mn}^{\text{III}}$ coordination compounds, prepared from the $\text{Ba}[\text{Pt}(\text{CN})_4]$ and $[\text{Mn}(\text{L4A/B})(\text{Cl})]$ (**1a/b**) precursor complexes, are reported. The polymeric complex $[\{\text{Mn}(\text{L4A})\}_2\{\mu^4\text{-Pt}(\text{CN})_4\}]_n$ (**2a**), where $\text{H}_2\text{L4A} = N,N'$ -ethylene-bis(salicylideneimine), comprises the $\{\text{Mn}(\text{L4A})\}$ moieties covalently connected through the $[\text{Pt}(\text{CN})_4]^{2-}$ bridges, thus forming a square-grid polymeric structure with the hexacoordinate Mn^{III} atoms. The trinuclear complex $[\{\text{Mn}(\text{L4B})\}_2\{\mu\text{-Pt}(\text{CN})_4\}]$ (**2b**), where $\text{H}_2\text{L4B} = N,N'$ -benzene-bis(4-aminodiethylene-salicylideneimine), consists of two $[\{\text{Mn}(\text{L4B})\}]$ moieties, involving pentacoordinate Mn^{III} atoms, bridged through the tetracyanidoplatinate (II) bridges to which they are coordinated in a *trans* fashion. Both complexes possess uniaxial type of magnetic anisotropy, with D (the axial parameter of zero-field splitting) = $-3.7(1)$ in **2a** and $-2.2(1) \text{ cm}^{-1}$ in **2b**. Furthermore, the parameters of magnetic anisotropy **2a** and **2b** were also thoroughly studied by theoretical complete active space self-consistent field (CASSCF) methods, which revealed that the former is much more sensitive to the ligand field strength of the axial ligands.

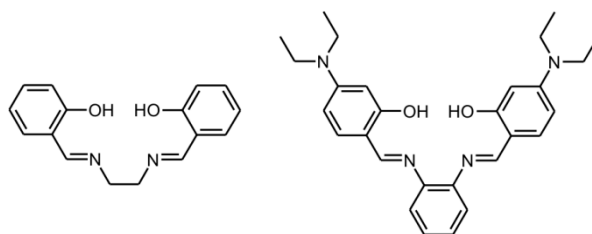
Keywords: manganese(III); platinum(II); zero-field splitting; magnetic anisotropy; crystal structures

1. Introduction

Single-molecule magnets (SMMs) are compounds composed of the individual molecules capable of preserving their magnetic moment even after removing external magnetic field. This is possible due to an existence of energy barrier Δ separating the states (formed by the crystal-field splitting of the ground spin state S , $S > 1/2$) with minimal and maximal M_S under the condition of axial magnetic anisotropy. The potential applications of SMMs and their polymeric analogues, so called single-chain magnets (SCMs), include information processing, data storage, quantum computing, spintronics, or biomedical applications [1,2].

Bearing in mind the above mentioned conditions for SMM occurrence it is clear why so much of attention has been devoted to the research of the Mn^{III} complexes involving tetradentate salen-type Schiff base ligands (e.g., $\text{L4A}^{2-} = \text{salen}^{2-} = N,N'$ -ethylene-bis(salicylideneimine) dianion; variously substituted salen ligands will be further abbreviated as $\text{H}_2\text{L4}$). In compounds involving the $[\text{Mn}(\text{L4})]^+$ moieties the central Mn^{III} atom is in the hexacoordinate environment and, thus, it is the object of the Jahn-Teller effect ($S = 2$, ${}^5\text{E}$ crystal field ground term in weak ligand fields). This implies distortion of the coordination polyhedron (its prolongation or compression), which gives rise to significant magnetic anisotropy. These might be of axial (prolongation) or easy-plane (compression) character [3]. Thus, it is clear that compounds of this type are attractive building blocks

for synthesis of 0D, 1D, 2D, or 3D coordination compounds exhibiting magnetic bistability [4,5]. A typical approach for synthesis of polymeric or polynuclear coordination compounds involving the $[\text{Mn}(\text{L4})]^+$ moieties is associated with the reaction of the halide precursor complexes $[\text{Mn}(\text{L4X})]$, where X = the halido ligand, with various cyanidometallates. Such reactions lead to preparations of compounds related to Prussian blue [6–11]. Previously, we reported on crystal structures and magnetic properties of polymeric and polynuclear compounds involving the $[\text{Mn}(\text{L4})]^+$ moieties which were bridged by $[\text{Fe}(\text{CN})_5(\text{NO})]^{2-}$, $[\text{Pt}(\text{SCN})_4]^{2-}$ and $[\text{Pt}(\text{SCN})_6]^{2-}$ complex anions [12–14]. This work represents a continuation of our ongoing study of platinum cyanido/thiocyanido bridged heterometallic compounds and reports on two new $\text{Mn}^{\text{III}}\dots\text{Pt}^{\text{II}}$ compounds involving the $[\text{Pt}(\text{CN})_4]^{2-}$ bridges: i.e., $[\{\text{Mn}(\text{L4A})\}_2\{\mu_4\text{-Pt}(\text{CN})_4\}]_n$ (**2a**) and $[\{\text{Mn}(\text{L4B})\}_2\{\mu\text{-Pt}(\text{CN})_4\}]$ (**2b**), where $\text{H}_2\text{L4B} = N,N'$ -benzene-bis(4-aminodiethylenesalicylideneimine) (Scheme 1). The prepared complexes were characterized by elemental analysis, molar conductivity, infrared spectroscopy, single crystal X-ray analysis, and magnetic measurements. To the best of our knowledge this is the first report on the crystal structures and magnetic properties of $\text{Mn}^{\text{III}}\dots\text{Pt}^{\text{II}}\dots\text{Mn}^{\text{III}}$ compounds involving $[\text{Pt}(\text{CN})_4]^{2-}$ as bridging units. Furthermore, the CASSCF/NEVPT2 calculations were performed on **2a** and **2b** and also on other model hexa/penta-coordinate compounds with the aim to more deeply understand variations in zero-field splitting (ZFS) parameters in Mn^{III} Schiff-base complexes.



Scheme 1. Schematic representations of the tetradentate Schiff base ligands: $\text{H}_2\text{L4A}$ (left), $\text{H}_2\text{L4B}$ (right).

2. Results

2.1. Crystal Structures

The crystal structures of **2a** and **2b** were determined by single-crystal X-ray analysis (Figure 1, Table 1). Both compounds comprise Pt^{II} atoms coordinated by four carbon atoms from the cyanide groups, thus forming a $\{\text{PtC}_4\}$ chromophore (Figure 1). The Pt–C bond lengths are from the narrow range of 1.99–2.00 Å (Figure 1), and with the C–Pt–C angles close to the ideal straight angle as expected for the square planar chromophore geometry ($179.6(5)^\circ$ in **2a**, and 180° in **2b**). In both compounds, the Schiff base ligands (Scheme 1) coordinate Mn^{III} atoms by two imino nitrogen (N_{im}) and two phenolate oxygen atoms with the metal–donor atom distances: $\text{Mn}-\text{N}_{\text{im}} = 1.96\text{--}1.98$ Å and $\text{Mn}-\text{O} = 1.86\text{--}1.89$ Å.

Table 1. Crystal data and structure refinements for **2a** and **2b**.

	2a	2b
Formula	$\text{C}_{36}\text{H}_{28}\text{Mn}_2\text{N}_8\text{O}_4\text{Pt}$	$\text{C}_{30}\text{H}_{32}\text{Mn}_6\text{O}_2\text{Pt}_{0.50}$
Mr	941.62	661.10
Space group	$P4/ncc$	$P-1$
Crystal system	tetragonal	triclinic
$a/\text{Å}$	14.7755(3)	10.6904(4)
$b/\text{Å}$	14.7755(3)	12.6273(3)
$c/\text{Å}$	16.7105(5)	13.2804(3)
$\alpha/^\circ$	90	70.773(2)
$\beta/^\circ$	90	79.588(2)
$\gamma/^\circ$	90	67.676(3)

Table 1. Cont.

	2a	2b
$V/\text{\AA}^3$	3648.2(2)	1562.69(9)
T/K	150(2)	150(2)
$D_C/\text{g cm}^{-3}$	1.717	1.405
μ/mm^{-1}	4.568	2.684
$F(000)$	1846.0	668.0
Reflections collected/unique	1612/1435	5396/4748
Data/restraints/parameters	1612/1/115	5396/0/361
Goodness of fit (GOF) on F^2	1.307	1.004
R_1, wR_2 ($I > 2\sigma(I)$) ^{a,b}	0.0500/0.1166	0.0368/0.0817
R_1, wR_2 (all data) ^{a,b}	0.0544/0.1166	0.0425/0.0829
CCDC number	1510379	1510378

$$^a R_1 = \sum(|F_o| - |F_c|) / \sum |F_o|; ^b wR_2 = \{\sum[w(F_o^2 - F_c^2)^2] / \sum[w(F_o^2)^2]\}^{1/2}.$$

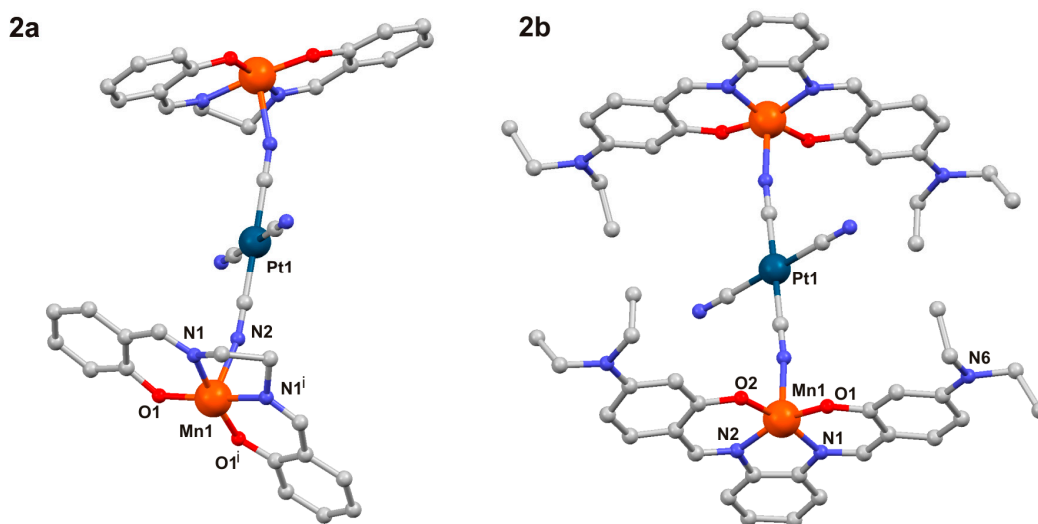


Figure 1. Part of crystal structure of **2a** (left) and molecular structure of **2b** (right). Hydrogen atoms are omitted due to clarity. Selected bond lengths (in Å) and angles ($^\circ$): **2a**: Mn1–N1 = 1.963(9), Mn1–N2 = 2.279(8), Mn1–O1 = 1.888(6), O1–Mn1–N1 = 173.1(3), N2–Mn1–N2ⁱ = 174.0(4), [Symmetry code: (i) $-y, -x, -z + 1/2$]; **2b**: Mn1–N1 = 1.974(3), Mn1–N2 = 1.976(3), Mn1–N3 = 2.192(4), Mn1–O1 = 1.879(3), Mn1–O2 = 1.868(3), O1–Mn1–N2 = 168.97(13), O2–Mn1–N1 = 161.89(14).

Crystal structure of **2a** is isostructural to the previously reported compound $[\text{Mn}(\text{L4A})\{\mu^4\text{-Ni}(\text{CN})_4\}]_n$ [15]. The N_{im} and O donor atoms form the equatorial plane of the coordination polyhedron of the Mn^{III} center, while the axial coordination sites are occupied by two symmetrically equivalent nitrogen atoms (N_{CN}) from bridging $[\text{Pt}(\text{CN})_4]^{2-}$ anions. Thus, the Mn^{III} atom is hexacoordinate with the $\{\text{MnN}_2\text{N}'_2\text{O}_2\}$ chromophore. The Mn– N_{CN} bond lengths are significantly longer than the Mn– N_{im} bonds due to a Jahn-Teller distortion: Mn– N_{CN} = 2.279(8) Å. Each $[\text{Pt}(\text{CN})_4]^{2-}$ bridging anion bonds to four $[\text{Mn}(\text{L4A})]^+$ moieties forming thus a square grid architecture and therefore, the overall crystal structure of **2a** can be classified as a two-dimensional polymer (Figure 2). The neighboring $[\text{Mn}(\text{L4A})\{\mu^4\text{-Pt}(\text{CN})_4\}]_n$ layers are weakly interconnected by the offset π – π stacking [16–18] of aromatic rings (the shortest C...C distance is 3.319(7) Å).

In **2b**, the *trans*-cyanido ligands of the $[\text{Pt}(\text{CN})_4]^{2-}$ bridges bond to the Mn^{III} atoms, thus forming trinuclear $[\{\text{Mn}(\text{L4B})\}\{\mu\text{-Pt}(\text{CN})_4\}]$ complex molecules (Figure 1). One axial position on each Mn^{III} center is unoccupied and, thus, the chromophore is pentacoordinate $\{\text{MnN}_2\text{N}'\text{O}_2\}$ with the coordination geometry close to ideal square pyramidal ($\tau = 0.12$) [19]. The Mn– N_{CN} distance in **2b** (2.193(4) Å) is significantly shorter than in **2a** (2.279(3) Å).

The reason for such difference is that the pentacoordinate Mn^{III} center in **2b** is not affected by Jahn-Teller effect. Furthermore, it must be stressed that the Mn^{III} atom is involved into metal... π non-covalent interactions with carbon atoms from aromatic part of the L4B²⁻ ligands from the adjacent trinuclear complex molecules (Figure 2). The Mn...C distances in such non-covalent contact are shorter (3.423(4) and 3.449(4) Å) than the sum of their van der Waals radii (3.7 Å) [20]. Other non-covalent interactions presented in **2b** are of π - π stacking nature. They do extend the crystal structure of **2b** to 2D supramolecular layers (Figure 2). Two different stacking interactions can be distinguished: (a) intrachain, π_1 - π_1 , with the shortest C...C distance at 3.338(5) Å, and (b) interchain, π_2 - π_2 , with the shortest C...C distance of 3.403(5) Å (Figure 2).

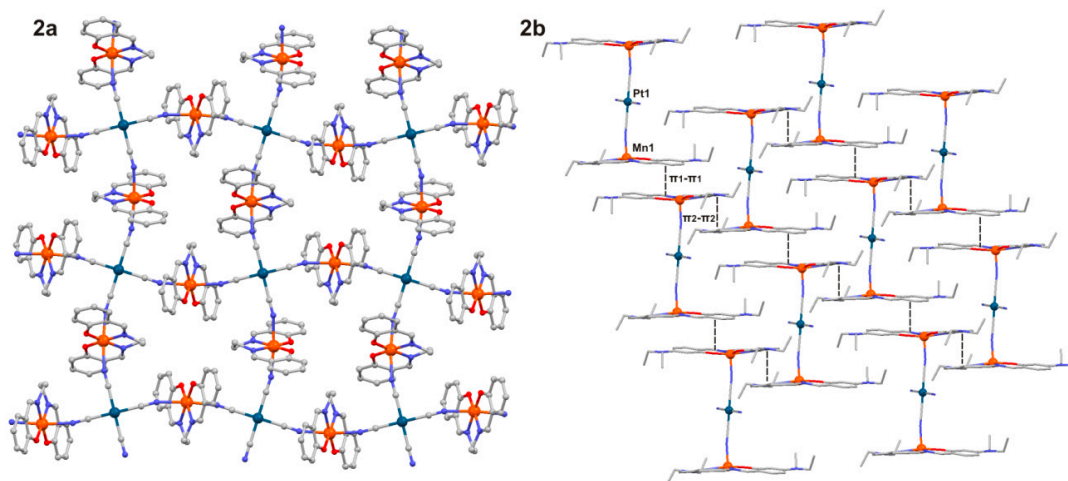


Figure 2. Fragments of the crystal structures of the complexes **2a** and **2b**. The hydrogen atoms are omitted for clarity. Several π - π stacking are displayed in the complex **2b** (black dashed lines).

2.2. Magnetic Properties

The magnetic data of complexes **2a** and **2b** are depicted in Figure 3 and conform with practically isolated paramagnetic Mn^{III} cations. The effective magnetic moment is linearly decreasing from the room temperature value of 4.91 μ_B to the value of 4.78 μ_B at 30 K for **2a**, and from 5.35 μ_B to the value of 4.89 μ_B at 30 K for **2b**. The decrease of the effective magnetic moment in this temperature region is much more apparent for **2b** and this can be ascribed to a presence of small amount of unknown magnetic impurity undetectable by other physical methods. Then, the effective magnetic moment drops to the value of 3.53 μ_B for **2a** and to the value of 4.19 μ_B for **2b** at the lowest available temperature ($T = 1.9$ K). This is mainly due to the zero-field splitting (ZFS) of Mn^{III} atoms and partly also due to very weak intra/inter-molecular non-covalent interactions. Therefore, we postulated the following spin Hamiltonian:

$$\hat{H} = D \left(\hat{S}_z^2 - \hat{S}^2/3 \right) + \mu_B B g \hat{S}_a - zj \langle \hat{S}_a \rangle \hat{S}_a \quad (1)$$

where the first term describes the magnetic anisotropy with single-ion axial ZFS parameter D , the second term is the Zeeman term, and the last term, represented with the zj variable, is the common molecular-field correction parameter, which is due to intermolecular interactions. The $\langle S_a \rangle$ is a thermal average of the molecular spin projection in the a direction of magnetic field defined as $B_a = B \cdot (\sin\theta\cos\varphi, \sin\theta\sin\varphi, \cos\theta)$ with the help of polar coordinates. Then, the molar magnetization in the a -direction of magnetic field can be numerically calculated as:

$$M_a = -N_A \frac{\sum_i \left(\sum_k \sum_l C_{ik}^+ (Z_a) C_{li} \right) \exp(-\varepsilon_{a,i}/kT)}{\sum_i \exp(-\varepsilon_{a,i}/kT)} \quad (2)$$

where Z_a is the matrix element of the Zeeman term for the a -direction of the magnetic field and C are the eigenvectors resulting from the diagonalization of the complete spin Hamiltonian matrix. The presence of z_j means that iterative procedure must be used [21]. Then, the averaged molar magnetization of the powder sample was calculated as integral (orientational) average:

$$M_{\text{mol}} = 1/4\pi \int_0^{2\pi} \int_0^\pi M_a \sin\theta d\theta d\varphi \quad (3)$$

In order to obtain reliable parameters, both temperature and field dependent magnetic data were fitted simultaneously, which resulted in these parameters: $D = -3.7(1) \text{ cm}^{-1}$, $g = 1.981(6)$, $z_j = -0.244(9) \text{ cm}^{-1}$, $\chi_{\text{TIM}} = 6(1) \cdot 10^{-9} \text{ m}^3 \cdot \text{mol}^{-1}$ for **2a**, and $D = -2.2(1) \text{ cm}^{-1}$, $g = 1.975(8)$, $z_j = -0.02(1) \text{ cm}^{-1}$, $\chi_{\text{TIM}} = 28(2) \cdot 10^{-9} \text{ m}^3 \cdot \text{mol}^{-1}$ for **2b**, where the temperature-independent magnetism correction χ_{TIM} was applied to describe the contribution of traces of magnetic impurities [22]. The sign of D -parameters suggests that in **2a** and **2b** there is axial magnetic anisotropy and that more negative D value found for **2a** revealed larger anisotropy in the hexacoordinate Mn^{III} compound as compared to that of pentacoordinate one.

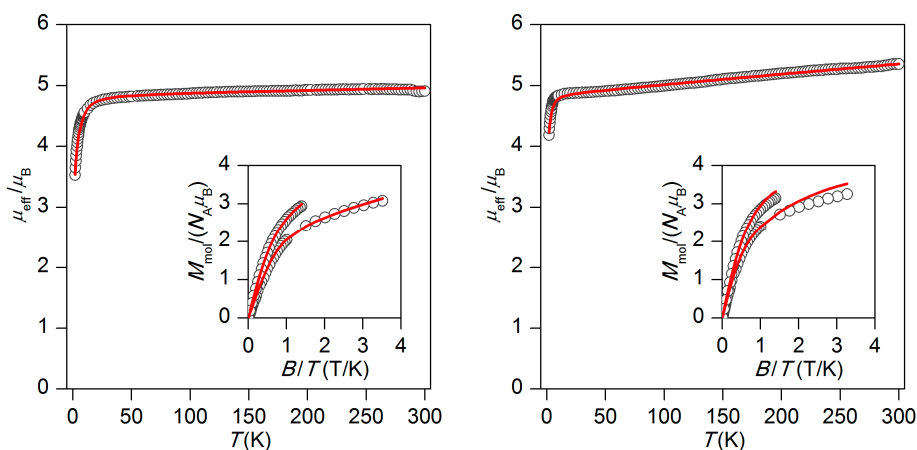


Figure 3. The magnetic data for **2a** (left) and **2b** (right) showing the temperature dependence of the effective magnetic moment calculated from the molar magnetization measured at $B = 0.1 \text{ T}$, and the reduced isothermal magnetizations measured at $T = 2$ and 5 K . Empty circles—experimental data, full lines—calculated data, using Equation (1), and $D = -3.7(1) \text{ cm}^{-1}$, $g = 1.981(6)$, $z_j = -0.244(9) \text{ cm}^{-1}$, $\chi_{\text{TIM}} = 6(1) \cdot 10^{-9} \text{ m}^3 \cdot \text{mol}^{-1}$ for **2a** and $D = -2.2(1) \text{ cm}^{-1}$, $g = 1.975(8)$, $z_j = -0.02(1) \text{ cm}^{-1}$, $\chi_{\text{TIM}} = 28(2) \cdot 10^{-9} \text{ m}^3 \cdot \text{mol}^{-1}$ for **2b**.

2.3. Theoretical Calculations

Furthermore, we supported our experimental magnetic study also by ab initio CASSCF/NEVPT2 calculations using ORCA computational package where also the relativistic effects were included as described in the Section 4.2.3. The resulting values of ZFS parameters were as follows: $D = -3.57 \text{ cm}^{-1}$ and $E/D = 0.030$ for **2a**, and $D = -2.75 \text{ cm}^{-1}$ and $E/D = 0.021$ for **2b**, while the components of g -tensors for both compounds were in narrow range from 1.977 to 1.994. Thus, the calculations supported our conclusions following from the experimental results showing that there is lower magnetic anisotropy in the pentacoordinate complex **2b** than in the hexacoordinate one (**2a**).

3. Discussion

In order to improve our understanding of magnetic anisotropy in these complexes, we performed magneto-structural correlations for pentacoordinate $[\text{Mn}(\text{L4A})(\text{MeCN})]^+$ (MnL_5) and hexacoordinate $[\text{Mn}(\text{L4A})(\text{MeCN})_2]^+$ (MnL_6) model compounds, where we studied the impact of axial ligand(s) field strength on ZFS parameters by varying $\text{Mn}-\text{N}_{\text{MeCN}}$ distance(s) from 1.9 to 2.8 Å (MeCN

= acetonitrile). The geometries of the complexes were optimized with the PBE functional also incorporating the COSMO model (COSMO = COnductor-like Screening MOdel). The only geometrical constrain applied was Mn–N_{MeCN} distance and in case of hexacoordinate MnL₆ model compound, the Mn–N_{MeCN} distances were both equal. Subsequently, the single-point energy calculations were done for each optimized geometry using B3LYP/ZORA/def2-TZVP(-f) followed by extracting the information about the splitting of *d*-orbitals, which is visualized in Figure 4 (top). This figure resembles the well-known crystal-field theory schemes outlined also in Figure 4 (bottom). In the case of hexacoordinate MnL₆ model compound with $d(\text{Mn-N}_{\text{MeCN}}) = 1.9 \text{ \AA}$, the *d*-orbitals are evidently split according to scheme outlined for a compressed square-bipyramidal coordination geometry, whereas for increasing Mn–N_{MeCN} distance, the pattern for elongated square-bipyramidal arrangement is observed. Upon further increase in the Mn–N_{MeCN} distance, the *d*-orbitals are split similarly to square-planar geometry. An analogous situation can be found for the pentacoordinate MnL₅ model compound, where an increase in the Mn–N_{MeCN} distance follows *d*-orbitals splitting from square-pyramidal to square-planar geometry. Of course, DFT-calculated (DFT = Density Functional Theory) energies of *d*-orbitals are not exactly following simplified schemes derived from the crystal-field theory due to non-equivalent ligand field strengths of Schiff base nitrogen and oxygen donor atoms. Then, ZFS parameters for each geometry were calculated by the same procedure with the CASSCF/NEVPT2 method. The results are depicted in Figure 5.

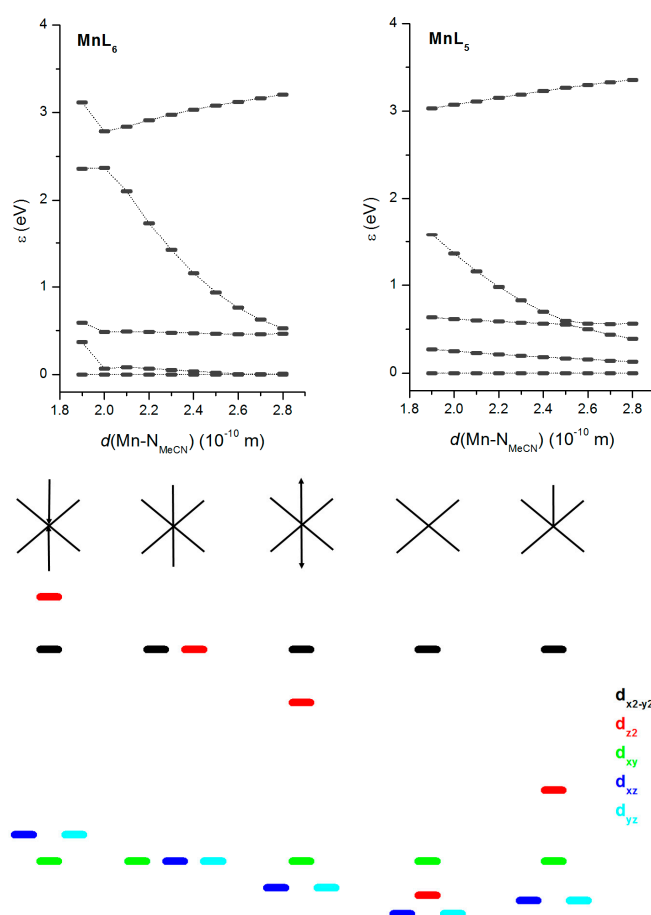


Figure 4. Top: the calculated *d*-orbitals energy splitting for the model compounds [Mn(L4A)(MeCN)]⁺ (MnL₆) and [Mn(L4A)(MeCN)₂]⁺ (MnL₅) for varying Mn–N_{MeCN} distance(s) from 1.9–2.8 Å using B3LYP/ZORA/def2-TZVP(-f); Bottom: variation of *d*-orbitals energy according to the crystal-field theory for idealized geometries (compressed square-bipyramid, octahedral, elongated square-bipyramid, square-planar, and square-pyramidal).

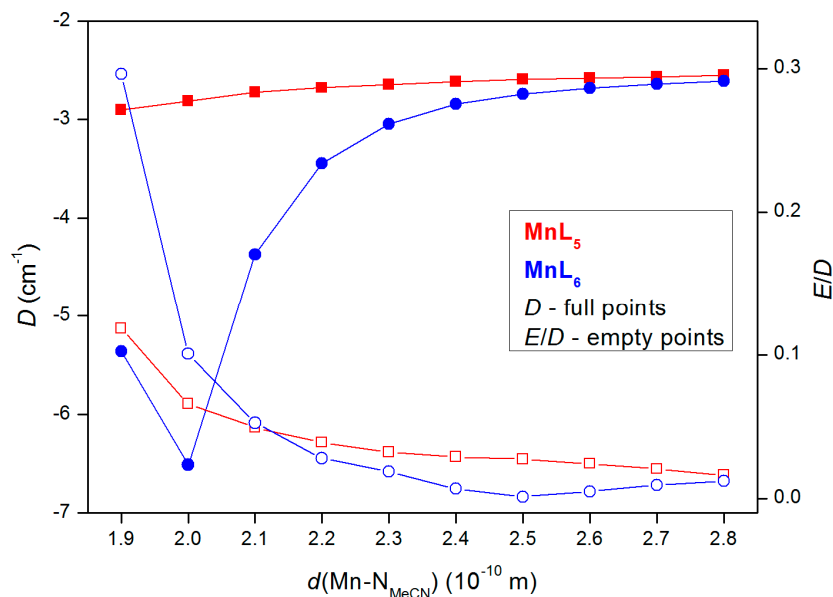


Figure 5. The CASSCF/NEVPT2 calculated magneto-structural correlation of ZFS parameters D and E for pentacoordinate $[\text{Mn}(\text{L4A})(\text{MeCN})]^+$ (MnL_5) and hexacoordinate $[\text{Mn}(\text{L4A})(\text{MeCN})_2]^+$ (MnL_6) model compounds for varying $\text{Mn-N}_{\text{MeCN}}$ distance(s) from 1.9–2.8 Å.

It is evident that there is a negligible effect of the axial ligand strength on magnetic anisotropy in the case of the pentacoordinate MnL_5 complex, the D varied only between -2.9 and -2.5 cm^{-1} . This is in the stark contrast with the hexacoordinate MnL_6 complex, where shortening of the Mn-N distances (axial elongation \rightarrow nearly ideal octahedron), in other words, increasing the ligand field strength of the axial ligands, led to immense increase of the negative value of the D -parameter ($D = -2.6 \rightarrow -6.5 \text{ cm}^{-1}$) with the maximal absolute value at the chromophore geometry close to the ideal octahedral arrangement (Figure 5). Further increase in the axial ligand field strength (i.e., the axial compression) would lead to crossover to compressed square-bipyramid and consequently to a positive value of the D -parameter, which is evidenced here by increase of E/D ratio approaching the value of $1/3$ (Figure 5). Such a relationship between the sign of D and the axial elongation/compression was already proposed by Maurice et al. for a simple $[\text{Mn}(\text{NCH})_6]^{3+}$ model complex [23]. Furthermore, we plotted the ligand field terms, quintets and triplets, arising from CASSCF/NEVPT2 calculations for both MnL_5 and MnL_6 model compounds (Figure 6). It is evident that the increase in the axial ligand field strength induced by decreasing of $\text{Mn-N}_{\text{MeCN}}$ distances led to significant lowering of the excited quintets and especially triplet states for MnL_6 , whereas energies of excited triplets and quintets states are not varied to such extent for MnL_5 . This different behaviour had dominant impact on the value of the D -parameter, because the contribution of quintet states to D is more or less the same for all $\text{Mn-N}_{\text{MeCN}}$ distances and moreover for both hexa- and pentacoordinate model complexes (Figure 6). Furthermore, the comparison of D -values for MnL_6 and MnL_5 model compounds at $d(\text{Mn-N}_{\text{MeCN}}) = 2.2\text{--}2.3 \text{ \AA}$ (Figure 5), that means for axial Mn-N distances found in **2a** and **2b**, clearly showed that more negative D is expected for hexacoordinate compound as also confirmed from the analysis of the experimental magnetic data of the reported compounds.

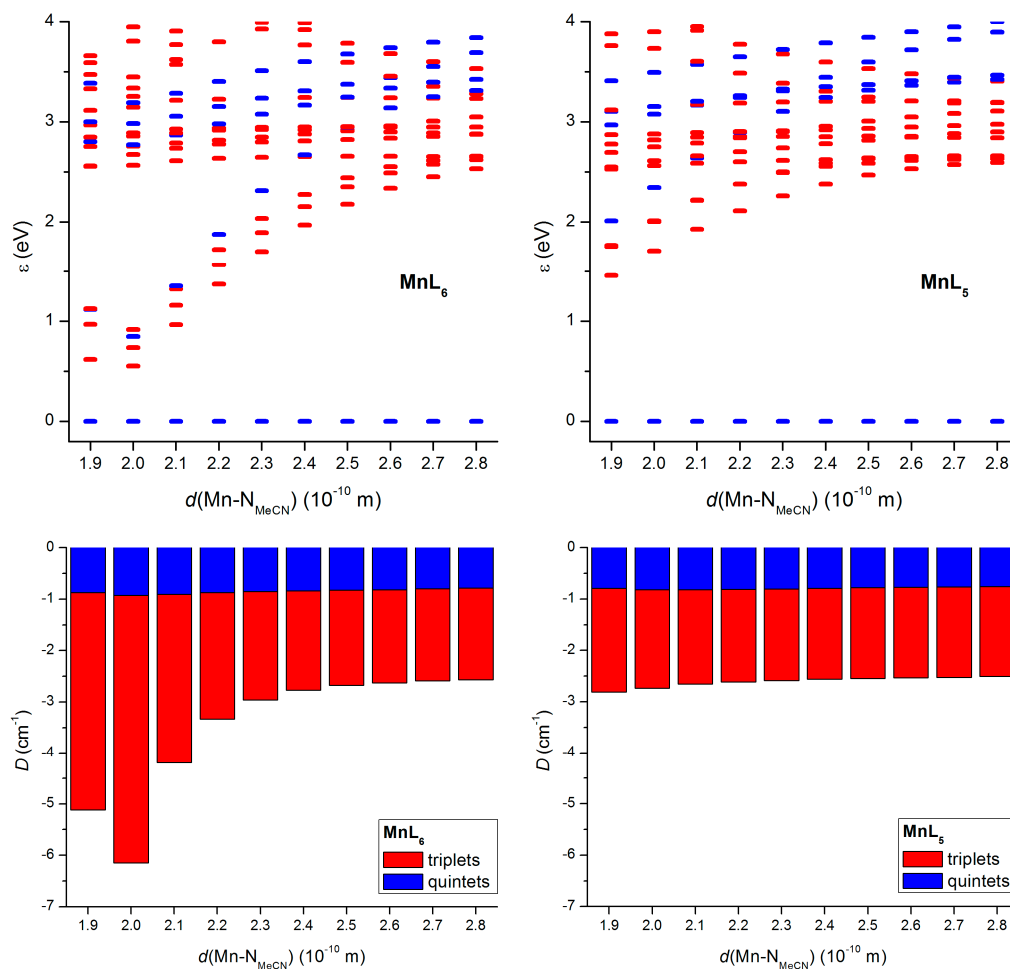


Figure 6. Top: ligand field terms arising from CASSCF/NEVPT2 calculations for the model compounds [Mn(L4A)(MeCN)]⁺ (MnL₅) and [Mn(L4A)(MeCN)₂]⁺ (MnL₆) done for varying Mn–N_{MeCN} distance(s) from 1.9–2.8 Å. Quintet states are blue and triplet states are red; Bottom: the contribution of quintet (blue) and triplet (red) states to the calculated *D*-parameter.

4. Materials and Methods

4.1. Materials

All of the starting chemicals were of analytical reagent grade and were used as received. All of the chemicals were purchased from commercial sources (Sigma Aldrich, St. Louis, MO, USA).

4.1.1. Preparation of Ba[Pt(CN)₄]

A solution of PtCl₂ (1 mmol, in 10 mL of water) was added to a cold, saturated solution of KCN (4 mmol, in 2 mL of water). The precipitated K₂[Pt(CN)₄]·3H₂O was filtered off. To the solution of K₂[Pt(CN)₄]·3H₂O (1 mmol, in 5 mL of water) the solution of BaCl₂ (1 mmol, in 3 mL of water) was added. The resulting green precipitate was filtered off, washed with diethyl ether and stored in a desiccator. Yield: 89%. Elem. anal. Calcd (%) for C₄N₄Ba₁Pt₁: C, 11.00; N, 12.83. Found: C, 11.33; N, 12.65. FT-IR data (ν_{\max} (ATRd)/cm⁻¹): 3512 w; 3270 w; 2653 w; 2596 w; 2286 w; 2120 vs ν (C≡N); 1982 w; 1653 w; 1618 m; 733; 561 w.

4.1.2. Preparation of $[\{\text{Mn}(\text{L4A})\}_2\{\mu^4\text{-Pt}(\text{CN})_4\}]_n$ (**2a**), and $[\{\text{Mn}(\text{L4B})\}_2\{\mu\text{-Pt}(\text{CN})_4\}]$ (**2b**)

The precursor complexes $[\text{Mn}(\text{L4A})\text{Cl}]$, **1a**, and $[\text{Mn}(\text{L4B})\text{Cl}]$, **1b**, were prepared according to the procedures in the literature [24].

A water solution (10 mL) of $\text{Ba}[\text{Pt}(\text{CN})_4]$ (0.1 mmol) was added under continuous stirring to a methanol solution (10 mL) of $[\text{Mn}(\text{L4A/B})\text{Cl}]$ **1a/b** (0.2 mmol). The reaction mixture was stirred for 60 min at room temperature, and then was kept undisturbed in the dark. After twelve days, single-crystals suitable for X-ray analysis were formed. The resulting crystals were filtered off from the mother liquor, washed with water, diethyl ether, dried in a drying kiln (at 50 °C), and stored in a desiccator.

2a: Yield: 85%. Elem. anal. Calcd (%) for $\text{C}_{36}\text{H}_{28}\text{N}_8\text{O}_4\text{Mn}_2\text{Pt}_1$: C, 45.91; H, 2.99; N, 11.90. Found: C, 45.86; H, 2.74; N, 12.26. FT-IR (ATR/ cm^{-1}): 594 m; 588 m; 550 w; 502 w; 456 s; 433 m; 379 s; 353 m; 341 m; 318 m; 296 m $\nu(\text{Mn-N})$; 247 w $\nu(\text{Mn-O})$; 210 w. FT-IR (KBr/ cm^{-1}): 3103 w; 3044 w $\nu(\text{C-H})_{\text{ar}}$; 2958 w $\nu(\text{C-H})_{\text{alip}}$; 2952 w $\nu(\text{C-H})_{\text{alip}}$; 2626 w; 2142s $\nu(\text{C}\equiv\text{N})$; 1982 w; 1625 vs $\nu(\text{C=N})_{\text{ar}}$; 1596 m, 1538 m, 1465 m $\nu(\text{C=C})_{\text{ar}}$; 1441 m; 1389 w; 1328 w; 1287 m; 1238 w; 1199 w; 1146 w; 1127 w; 1084 w; 1049 w; 1029 w; 901 w; 862 w; 795 w; 764 w; 647 w.

2b: Yield: 81%. Elem. anal. Calcd (%) for $\text{C}_{60}\text{H}_{64}\text{N}_{12}\text{O}_4\text{Mn}_2\text{Pt}_1$: C, 54.50; H, 4.87; N, 12.71. Found: C, 54.71; H, 4.68; N, 12.89. FT-IR (ATR/ cm^{-1}): 577 w; 538 w; 529 w; 520 w; 499 w; 482 w; 462 w; 438 w; 421 w; 400 w; 355 w; 345 w; 316 w; 288 w, 258 w. FT-IR data (KBr/ cm^{-1}): 3288 w; 3078 w $\nu(\text{C-H})_{\text{ar}}$; 2972 w $\nu(\text{C-H})_{\text{alip}}$; 2229 w $\nu(\text{C-H})_{\text{alip}}$; 2757 w; 2142 s $\nu(\text{C}\equiv\text{N})$; 1609s $\nu(\text{C=N})_{\text{ar}}$; 1559 m, 1516 m, 1486 m $\nu(\text{C=C})_{\text{ar}}$; 1431 w; 1412 w; 1374 w; 1334 w; 1310 w; 1276 w; 1244 m; 1208 w; 1189 w; 1170 w; 1139 w; 1076 w; 1039 w; 1019 w; 965 w; 825 w; 787 m; 741 m; 701 w; 650 w.

4.2. Methods

4.2.1. General Methods

Elemental analysis (CHN) was performed on a FLASH 2000 CHN Analyser (ThermoFisher Scientific, Waltham, MA, USA). Infrared spectra of the complexes were recorded on a NEXUS 670 FT-IR spectrometer (Thermo Nicolet, Waltham, MA, USA) using the ATR technique on a diamond plate in the range 600–4000 cm^{-1} . The reported FT-IR intensities were defined as w = weak, m = medium, s = strong, and vs = very strong. The magnetic data were measured on powdered samples pressed into pellets using a MPMS XL-7 Quantum Design SQUID magnetometer (Quantum Design Inc., San Diego, CA, USA). The experimental data were corrected for the diamagnetism of the constituent atoms by using Pascal's constants.

4.2.2. Single Crystal X-ray Analysis Details

Single crystal X-ray diffraction data of **2a** and **2b** were collected on an Oxford diffractometer Xcalibur2 (Oxford Diffraction Ltd., Oxford, UK) with the Sapphire CCD detector and fine-focused sealed tube (Mo $K\alpha$ radiation, $\lambda = 0.71073 \text{ \AA}$) source and equipped with an Oxford Cryosystem nitrogen gas flow apparatus. All structures were solved by direct methods using SHELXS-2014 [25] incorporated into the WinGX program package [26]. For each structure, its space group was checked by the ADSYMM procedure with PLATON software [27,28]. All structures were refined using full-matrix least-square procedures on F^2 with SHELXL-2014 [25] with anisotropic displacement parameters for all non-hydrogen atoms. The hydrogen atoms were placed into the calculated positions and they were included into the riding model approximation, with $U_{\text{iso}} = 1.2$ or $1.5 U_{\text{eq}}$. All of the crystal structures were visualized using Mercury software [16].

4.2.3. Theoretical Methods

Ab initio CASSCF/NEVPT2 calculations [29,30] using ORCA 3.0 [31] with active space defined by four electrons in five d -atomic orbitals, CAS(4,5) and taking into account five quintets and

45 triplets. The relativistic effects were also included in the calculations with zero order regular approximation (ZORA) [32,33] together with the scalar relativistic contracted version of def2-TZVP(-f) basis functions [34]. The calculations utilized the RI approximation with the decontracted auxiliary def2-TZV/C Coulomb fitting basis sets and the chain-of-spheres (RIJCOSX) approximation to exact exchange [35]. Increased integration grids (Grid5 in ORCA convention) and tight SCF convergence criteria were used. The ZFS parameters, based on dominant spin-orbit coupling contributions from excited states, were calculated through quasi-degenerate perturbation theory (QDPT) [36], in which approximations to the Breit-Pauli form of the spin-orbit coupling operator (Spin-Orbit Mean-Field (SOMF) approximation) [37] and the effective Hamiltonian theory [38] were utilized.

The geometries of pentacoordinate $[\text{Mn}(\text{L4A})(\text{MeCN})]^+$ and hexacoordinate $[\text{Mn}(\text{L4A})(\text{MeCN})_2]^+$ model compounds were optimized with the PBE functional [39] again using the scalar relativistic contracted version of def2-TZVP(-f) basis functions incorporating the COSMO model [40]. The single-point energy calculations were done for each optimized geometry using B3LYP functional [41–43]. ZFS parameters were calculated by the same procedure with the CASSCF/NEVPT2 method described above.

5. Conclusions

In conclusion, this work presents synthesis and characterization of two new $\text{Mn}^{\text{III}}\dots\text{Pt}^{\text{II}}\dots\text{Mn}^{\text{III}}$ complexes with the general formula $[\{\text{Mn}(\text{L4A})\}_2\{\mu_4\text{-Pt}(\text{CN})_4\}]_n$ (**2a**) and $[\{\text{Mn}(\text{L4B})\}_2\{\mu\text{-Pt}(\text{CN})_4\}]$ (**2b**). Both compounds were investigated by single crystal X-ray diffraction and their magnetic properties were studied by temperature and field dependent measurements of magnetic moment. These studies revealed that compound **2a** has a two-dimensional polymeric structure with the hexacoordinate Mn^{III} atoms, while **2b** possesses a trimeric structure with both Mn^{III} atoms being pentacoordinate. The analysis of magnetic data showed that the magnetic anisotropy is uniaxial in both compounds, with $D = -3.7(1)$ for **2a** and $-2.2(1) \text{ cm}^{-1}$ for **2b**. These findings were also supported by CASSCF/NEVPT2 calculations ($D = -3.57 \text{ cm}^{-1}$ and $E/D = 0.030$ for **2a**, and $D = -2.75 \text{ cm}^{-1}$ and $E/D = 0.021$ for **2b**). Further theoretical modelling of other pentacoordinate $[\text{Mn}(\text{L4A})(\text{MeCN})]^+$ and hexacoordinate $[\text{Mn}(\text{L4A})(\text{MeCN})_2]^+$ model compounds elucidated why the axial ZFS parameter D is larger in the case of the latter. The next important consequence is that magnetic anisotropy cannot be practically tuned in pentacoordinate square-pyramidal complexes by modifying ligands in axial position. On the contrary, hexacoordinate square-bipyramidal complexes are sensitive to the axial ligand field, thus prone to tuning of magnetic anisotropy, and for that reason they indicate themselves as promising for the preparation of the single-molecule magnets (SMMs).

Acknowledgments: The authors gratefully acknowledge the institutional support from the Palacký University in Olomouc. The authors thank Tomáš Šilha for his help with the preparation of the complexes, and Jana Gálíková and Alena Klanicová for FT-IR spectra measurements.

Author Contributions: I.N., R.H. and Z.T. conceived and designed the experiments; I.N. and R.H. performed the experiments; I.N., R.H. and Z.T. analyzed the data; I.N., R.H. and Z.T. wrote the paper. All authors read and approved the final manuscript.

Conflicts of Interest: The authors declare no conflict of interest.

References and Notes

1. Miyasaka, H.; Saitoh, A.; Abe, S. Magnetic assemblies based on Mn(III) salen analogues. *Coord. Chem. Rev.* **2007**, *251*, 2622–2664. [[CrossRef](#)]
2. Wang, S.; Ding, X.-H.; Li, Y.-H.; Huang, W. Dicyanometalate chemistry: A type of versatile building block for the construction of cyanide-bridged molecular architectures. *Coord. Chem. Rev.* **2012**, *256*, 439–464. [[CrossRef](#)]
3. Herchel, R.; Váhovská, L.; Potočňák, I.; Trávníček, Z.K. Slow Magnetic Relaxation in Octahedral Cobalt(II) Field-Induced Single-Ion Magnet with Positive Axial and Large Rhombic Anisotropy. *Inorg. Chem.* **2014**, *53*, 5896–5898. [[CrossRef](#)] [[PubMed](#)]

4. Pedersen, K.S.; Bendix, J.; Clerac, R. Single-molecule magnet engineering: Building-block approaches. *Chem. Commun.* **2014**, *50*, 4396–4415. [[CrossRef](#)] [[PubMed](#)]
5. Nemeč, I.; Herchel, R.; Trávníček, Z.; Šilha, T. Field-induced slow relaxation of magnetization in dinuclear and trinuclear $\text{Co}^{\text{III}}\cdots\text{Mn}^{\text{III}}$ complexes. *RSC Adv.* **2016**, *6*, 3074–3083. [[CrossRef](#)]
6. Singh, S.K.; Vignesh, K.R.; Archana, V.; Rajaraman, G. Theoretical insights into the origin of magnetic exchange and magnetic anisotropy in $\{\text{Re}^{\text{IV}}\text{-M}^{\text{II}}\}$ (M = Mn, Fe, Co, Ni and Cu) single chain magnets. *Dalton Trans.* **2016**, *45*, 8201–8214. [[PubMed](#)]
7. Ababei, R.; Li, Y.-G.; Roubeau, O.; Kalisz, M.; Brefuel, N.; Coulon, C.; Harte, E.; Liu, X.; Mathoniere, C.; Clerac, R. Bimetallic cyanido-bridged magnetic materials derived from manganese(III) Schiff-base complexes and pentacyanonitrosylferrate(II) precursor. *New J. Chem.* **2009**, *33*, 1237–1248. [[CrossRef](#)]
8. Yoon, J.H.; Lim, J.H.; Kim, H.C.; Hong, C.S. Cyanide-Bridged Single-Molecule Magnet Constructed by an Octacoordinated $[\text{W}(\text{CN})_6(\text{bpy})]^-$ Anion. *Inorg. Chem.* **2006**, *45*, 9613–9615. [[CrossRef](#)] [[PubMed](#)]
9. Dreiser, J.; Schnegg, A.; Holldack, K.; Pedersen, K.S.; Schau-Magnussen, M.; Nehr Korn, J.; Tregenna-Piggott, P.; Mutka, H.; Weihe, H.; Bendix, J.; et al. Frequency-Domain Fourier-Transform Terahertz Spectroscopy of the Single-Molecule Magnet $(\text{NEt}_4)[\text{Mn}_2(5\text{-Brsalen})_2(\text{MeOH})_2\text{Cr}(\text{CN})_6]$. *Chem. Eur. J.* **2011**, *17*, 7492–7498. [[CrossRef](#)] [[PubMed](#)]
10. Pedersen, K.S.; Dreiser, J.; Nehr Korn, J.; Gysler, M.; Schau-Magnussen, M.; Schnegg, A.; Holldack, K.; Bittl, R.; Piligkos, S.; Weihe, H.; et al. A linear single-molecule magnet based on $[\text{Ru}^{\text{III}}(\text{CN})_6]^{3-}$. *Chem. Commun.* **2011**, *47*, 6918–6920. [[CrossRef](#)] [[PubMed](#)]
11. Hoeke, V.; Heidemeier, M.; Krickemeyer, E.; Stammer, A.; Bogge, H.; Schnack, J.; Glaser, T. Structural influences on the exchange coupling and zero-field splitting in the single-molecule magnet $[\text{Mn}^{\text{III}}_6\text{Mn}^{\text{III}}]^{3+}$. *Dalton Trans.* **2012**, *41*, 12942–12959. [[CrossRef](#)] [[PubMed](#)]
12. Šilha, T.; Nemeč, I.; Herchel, R.; Trávníček, Z. Structural and magnetic characterizations of the first manganese(III) Schiff base complexes involving hexathiocyanidoplatinate(IV) bridges. *CrystEngComm* **2013**, *15*, 5351–5358. [[CrossRef](#)]
13. Nemeč, I.; Šilha, T.; Herchel, R.; Trávníček, Z. Investigation of Magnetic Exchange Pathways in Heterotrinnuclear Manganese(III) Schiff Base Complexes Involving Tetrathiocyanidoplatinate(II) Bridges. *Eur. J. Inorg. Chem.* **2013**, *2013*, 5781–5789. [[CrossRef](#)]
14. Nemeč, I.; Herchel, R.; Šilha, T.; Trávníček, Z. Towards a better understanding of magnetic exchange mediated by hydrogen bonds in Mn(III)/Fe(III) salen-type supramolecular dimers. *Dalton Trans.* **2014**, *43*, 15602–15616.
15. Yuan, A.-H.; Shen, X.-P.; Wu, Q.-J.; Huang, Z.-X.; Xu, Z. Synthesis, Crystal Structure and Magnetic Properties of a Two-Dimensional Heterometallic Assembly $[\text{Mn}(\text{salen})]_2[\text{Ni}(\text{CN})_4] \cdot 1/2\text{H}_2\text{O}$. *J. Coord. Chem.* **2002**, *55*, 411–420. [[CrossRef](#)]
16. Meyer, E.A.; Castellano, R.K.; Diederich, F. Interactions with Aromatic Rings in Chemical and Biological Recognition. *Angew. Chem. Int. Ed.* **2003**, *42*, 1210–1250. [[CrossRef](#)] [[PubMed](#)]
17. Salonen, L.M.; Ellermann, M.; Diederich, F. Aromatic Rings in Chemical and Biological Recognition: Energetics and Structures. *Angew. Chem. Int. Ed.* **2011**, *50*, 4808–4842. [[CrossRef](#)] [[PubMed](#)]
18. Sinnokrot, M.O.; Sherrill, C.D. High-Accuracy Quantum Mechanical Studies of π - π Interactions in Benzene Dimers. *J. Phys. Chem. A* **2006**, *110*, 10656–10668. [[CrossRef](#)] [[PubMed](#)]
19. Addison, A.W.; Rao, T.N.; Reedijk, J.; van Rijn, J.; Verschoor, G.C. Synthesis, structure, and spectroscopic properties of copper(II) compounds containing nitrogen-sulphur donor ligands; the crystal and molecular structure of aqua[1,7-bis(N-methylbenzimidazol-2'-yl)-2,6-dithiaheptane]copper(II) perchlorate. *J. Chem. Soc. Dalton Trans.* **1984**, 1349–1356. [[CrossRef](#)]
20. Batsanov, S.S. Van der Waals Radii of Elements. *Inorg. Mater.* **2001**, *37*, 871–885. [[CrossRef](#)]
21. Boča, R. *Theoretical Foundations of Molecular Magnetism*; Elsevier: Amsterdam, The Netherlands, 1999.
22. The standard deviations of the fitted parameters were calculated as $\sigma_i = (P_{ii}^{-1} \cdot S / (N - k))^{-1/2}$, where $P_{ij} = \Sigma(\delta\mu_n / \delta a_i \cdot \delta\mu_n / \delta a_j)$ and $S = \Sigma(\mu_n - \mu_n^{\text{exp}})^2$ with $n = 1$ to N ; a_i and a_j are fitted parameters, N is number of experimental points (sum of temperature and field dependent data), μ_n and μ_n^{exp} are the calculated and experimental effective magnetic moments for given temperature and magnetic field. The σ_i was then multiplied by Student's $t_{95\%}$ to provide confidence limits with the 95% probabilities listed in the text.

23. Maurice, R.; de Graaf, C.; Guihéry, N. Magnetostructural relations from a combined ab initio and ligand field analysis for the nonintuitive zero-field splitting in Mn(III) complexes. *J. Chem. Phys.* **2010**, *133*, 084307. [[CrossRef](#)] [[PubMed](#)]
24. Ciringh, Y.; Gordon-Wylie, S.W.; Norman, R.E.; Clark, G.R.; Weintraub, S.T.; Horwitz, C.P. Multinuclear paramagnetic NMR spectra and solid state X-ray crystallographic characterization of manganese(III) Schiff-base complexes. *Inorg. Chem.* **1997**, *36*, 4968–4982. [[CrossRef](#)]
25. Sheldrick, G. Crystal structure refinement with SHELXL. *Acta Cryst. C* **2015**, *71*, 3–8. [[CrossRef](#)] [[PubMed](#)]
26. Farrugia, L. WinGX suite for small-molecule single-crystal crystallography. *J. Appl. Crystallogr.* **1999**, *32*, 837–838. [[CrossRef](#)]
27. Spek, A. Structure validation in chemical crystallography. *Acta Cryst. Section D* **2009**, *65*, 148–155. [[CrossRef](#)] [[PubMed](#)]
28. Le, Y. MISSYM1.1—A flexible new release. *J. Appl. Crystallogr.* **1988**, *21*, 983–984.
29. Malmqvist, P.-Å.; Roos, B.O. The CASSCF state interaction method. *Chem. Phys. Lett.* **1989**, *155*, 189–194.
30. Angeli, C.; Cimiraglia, R.; Evangelisti, S.; Leininger, T.; Malrieu, J.P. Introduction of n-electron valence states for multireference perturbation theory. *J. Chem. Phys.* **2001**, *114*, 10252–10264. [[CrossRef](#)]
31. Neese, F. The ORCA program system. *Wiley Interdiscip. Rev. Comput. Mol. Sci.* **2012**, *2*, 73–78. [[CrossRef](#)]
32. Van Lenthe, E.; Baerends, E.J.; Snijders, J.G. Relativistic regular two-component Hamiltonians. *J. Chem. Phys.* **1993**, *99*, 4597–4610. [[CrossRef](#)]
33. Van Wüllen, C. Molecular density functional calculations in the regular relativistic approximation: Method, application to coinage metal diatomics, hydrides, fluorides and chlorides, and comparison with first-order relativistic calculations. *J. Chem. Phys.* **1998**, *109*, 392–399. [[CrossRef](#)]
34. Pantazis, D.A.; Chen, X.-Y.; Landis, C.R.; Neese, F. All-Electron Scalar Relativistic Basis Sets for Third-Row Transition Metal Atoms. *J. Chem. Theory Comput.* **2008**, *4*, 908–919. [[CrossRef](#)] [[PubMed](#)]
35. Neese, F.; Wennmohs, F.; Hansen, A. Efficient and accurate local approximations to coupled-electron pair approaches: An attempt to revive the pair natural orbital method. *J. Chem. Phys.* **2009**, *13*, 114108. [[CrossRef](#)]
36. Ganyushin, D.; Neese, F. First-principles calculations of zero-field splitting parameters. *J. Chem. Phys.* **2006**, *125*, 024103. [[CrossRef](#)] [[PubMed](#)]
37. Neese, F. Efficient and accurate approximations to the molecular spin-orbit coupling operator and their use in molecular g-tensor calculations. *J. Chem. Phys.* **2005**, *122*, 034107. [[CrossRef](#)] [[PubMed](#)]
38. Maurice, R.; Bastardis, R.; Graaf, C.; Suaud, N.; Mallah, T.; Guihéry, N. Universal Theoretical Approach to Extract Anisotropic Spin Hamiltonians. *J. Chem. Theory Comput.* **2009**, *5*, 2977–2984. [[CrossRef](#)] [[PubMed](#)]
39. Perdew, J.P.; Burke, K.; Ernzerhof, M. Generalized gradient approximation made simple. *Phys. Rev. Lett.* **1996**, *77*, 3865–3868. [[CrossRef](#)] [[PubMed](#)]
40. Klamt, A.; Schuurmann, G. COSMO: A new approach to dielectric screening in solvents with explicit expressions for the screening energy and its gradient. *J. Chem. Soc. Perkin Trans.* **1993**, 799–805. [[CrossRef](#)]
41. Becke, A.D. Density-functional exchange-energy approximation with correct asymptotic behavior. *Phys. Rev. A* **1988**, *38*, 3098–3100. [[CrossRef](#)]
42. Lee, C.T.; Yang, W.T.; Parr, R.G. Development of the Colle-Salvetti correlation-energy formula into a functional of the electron density. *Phys. Rev. B* **1988**, *37*, 785–789. [[CrossRef](#)]
43. Stephens, P.J.; Devlin, F.J.; Chabalowski, C.F.; Frisch, M.J. Ab Initio Calculation of Vibrational Absorption and Circular Dichroism Spectra Using Density Functional Force Fields. *J. Phys. Chem.* **1994**, *98*, 11623–11627. [[CrossRef](#)]

Sample Availability: Samples of the compounds are not available from the authors.



© 2016 by the authors; licensee MDPI, Basel, Switzerland. This article is an open access article distributed under the terms and conditions of the Creative Commons Attribution (CC-BY) license (<http://creativecommons.org/licenses/by/4.0/>).